Characteristic Modes Analysis for Circularly Polarized 1-Bit Dual-Layer Transmitarray Design

FRANCESCO ALESSIO DICANDIA [ID][1] **(Member, IEEE), AND SIMONE GENOVESI** [ID][2] **(Senior Member, IEEE)**

[1]Istituto di Elettronica e di Ingegneria dell'Informazione e delle Telecomunicazioni, Consiglio Nazionale delle Ricerche, 56122 Pisa, Italy
[2]Dipartimento di Ingegneria dell'Informazione, Università di Pisa, 56122 Pisa, Italy

CORRESPONDING AUTHOR: F. A. DICANDIA (e-mail: francescoalessio.dicandia@cnr.it)

ABSTRACT   A novel approach for designing a circularly polarized (CP) transmitarray (TA) by resorting to the characteristic modes analysis (CMA) is presented. Two miniaturized dual-layer polarization-insensitive unit cells are tailored to provide the two copolar transmission coefficient phase states that act as a 1-bit spatial phase shifter in the TA. The exploitation of a pair of characteristic modes (CMs), radiating either right-handed CP (RHCP) or left-handed CP (LHCP) scattered field, is at the basis of the TA operation. The TA provides a forward CP scattered field ensuring a low copolar insertion loss (IL) as well as a copolar transmission phase difference of 0° or 180°. To validate the proposed CMA-inspired theoretical study, a CP 1-bit TA has been designed, simulated, fabricated and tested. Measurements assess a good agreement with simulations, showing a maximum TA gain of 21.8 dBic with a remarkable 3 dB gain bandwidth of 15.22 % (7.77 GHz - 9.05 GHz), a peak aperture efficiency of 28.5 % and a very low profile.

INDEX TERMS   Circular polarization, transmitarray, planar lens, characteristic modes (CMs).

I. INTRODUCTION

HIGH-GAIN antennas represent a pivotal feature for enabling wireless communications with the required quality of services (QoS) in most of the modern wireless systems and will represent a key factor in driving their evolution with the advent of future 6G wireless technologies [1]. Moreover, the exploitation of higher carrier frequencies such as millimeter wave (mmWave) or terahertz (THz) are envisioned to play a crucial position in coping the ever-increasing system requirements such as high data-throughput and improved energy efficiency for beyond 5G (B5G) and 6G systems [2], [3]. Nevertheless, high frequency bands undergo larger propagation loss and suffer the presence of obstacles that lead to considerable coverage limitation compared to sub-6 GHz communication systems [4]. Therefore, highly directive antennas turn out to be an essential component to counteract these drawbacks and fulfill the system needs, as well as enabling the realization of the next wireless communications technologies such as Internet of Everything (IoE), device to device (D2D), autonomous vehicles in addiction to a ubiquitous and seamless wireless connectivity [5]. In

this context, circularly polarized (CP) radiation represents another appealing asset in several applicative scenarios such as radio frequency identification [6], indoor propagation and space-based communications [7], [8] as well as non-terrestrial networks [9], [10].

The most traditional approach for fulfilling a very directive antenna is represented by phased arrays [11], [12]. However, their use is questioned in many applications by the related cost and power consumption, although some unconventional techniques with the purpose of providing a performance tradeoff between cost and radiative performance were designed [13], [14].

An alternative solution, in the framework of high-gain pencil beam antenna, is represented by transmitarrays (TAs), where sub-wavelength elements on a surface re-phase the impinging spherical wave and transmit it as a plane wave [15]. Indeed, as complementary solution to reflectors or lens antennas [16], [17], TAs provide several prominent advantages such as lightweight, easy fabrications process, low cost as well as the capability to adapt to conformal structures [18]. TAs are generally composed by planar unit

cells capable to transform the incident spherical wavefront coming from a primary feeder to an outgoing planar wavefront toward the desired direction (θ,φ). TAs represent an appealing solution in many applications spanning from satellites systems [19], [20], mobile communications [21], [22], [23] to radar applications [24] by providing a tailored phase shift profile without the significant insertion losses typical of arrays feeding networks.

One of the most straightforward ways to control the TA spatial phase profile is inspired to the cascade of multiple frequency selective surfaces (FSSs) layers [25], [26]. A FSS is capable of modifying the impinging electromagnetic wave characteristics such as magnitude and phase of the transmitted field, or its polarization status, by the periodic arrangement of a single unit cell [27], [28]. In the TA case, the transmission magnitude and phase of each element is controlled by varying the unit cells and over the past years several CP TA designs have been presented [19], [20], [29], [30], [31], [32]. However, they are based on the cascade of at least three conductive layers, printed on dielectric substrates or realized with metallic sheets separated by air gaps. Therefore, these solutions need both precise realization and accurate multilayers alignment as well as an efficient assembly that inevitably complicate the fabrication process and increase the manufacturing cost, especially at high frequencies. Thereby, one of the most challenging aspects consist of having a simple and low-profile TA geometry by employing the least number of FSS layers compliant with the system needs. It is worth noting that CP TA solutions comprising only two metallic layers have been presented in [33], [34], [35]. Nevertheless, the bulky size or the narrow frequency response make them not compliant to the required specifications in many applicative scenarios.

Among the several TA technologies, the ones that have a quantized phase resolution stand out since they, in general, guarantee larger working bandwidths, less complex design and fabrication, a certain suitability for implementing reconfigurability even though they exhibit lower aperture efficiency [36], [37], [38], [39], [40], [41]. Hence, from the radiative performance perspective, the selection of the phase correction scheme for a TA is a tradeoff between the achievable working bandwidth and the aperture efficiency. For example, a dual band 1-bit TA employing a polarization-converter spatial phase shifter is illustrated in [38]. A wideband and low cross-polarizations 1-bit TA has been designed in [39]. Dealing with CP TAs, some solutions are presented in [42], [43], [44], [45], [46], although they require at least three metallic layers. Therefore, the design of a low profile (lower than 0.1 λ) CP TA employing only two metallic layers has not been reported yet, despite various phase quantized-based solutions have been already proposed.

To this end, the purpose of this work is to propose a novel CP 1-bit TA, namely with two phase states, by exploiting a miniaturized polarization-insensitive transmitting unit

cells composed by two metallic layers only. Specifically, systematic design guidelines for the synthesis of the two compact unit cells are provided based on the scattered modal fields calculated with the characteristic mode analysis (CMA) [47]. More in detail, a unit cell supporting CP-radiating characteristic modes (CMs) with a CP handedness opposite to that of the primary CP feeder, turns out to be almost transparent. On the contrary, the exploitation of a unit cell supporting a pair of CMs radiating a CP field with the same handedness of the primary CP feeder is at the basis of a TA producing a forward CP scattering field liable for both a low copolar transmission insertion loss (IL) and a copolar transmission phase difference of 180°.

This paper is organized as follows. Section II highlights the required properties of the CP 1-bit TA in terms of its scattered field ($\underline{E}^s$). Section III is devoted to the identification of two kinds of scatterers capable of supporting CMs characterized by a CP radiation with a proper CP handedness by exploiting CMA. The following Section IV is paid to the design of CP 1-bit TA whereas Section V addresses the manufactured prototype and measurements. Finally, Section VI provides the conclusions.

II. FEATURES OF THE CP 1-BIT TA SCATTERED FIELD

A theoretical analysis aimed to derive both the operating principle and the required conditions of the CP 1-bit TA unit cells scattered field, $\underline{E}^s$, illuminated by a feeder with the same polarization is carried out in this section. To this end, let us consider a planar TA illuminated by an orthogonally incident left-handed CP (LHCP) plane wave, $\underline{E}^i$, propagating along z-axis. Thus, to realize a TA with 1-bit phase resolution, the designed transmitting unit cells must be able to generate a scattered field ($\underline{E}^s$) that, once added to the incident one ($\underline{E}^i$), provides the following transmitted wave ($\underline{E}^t$) propagating along z-axis:

$$\underline{E}^t = \underline{E}^i + \underline{E}^s = E_0\left(i_x + ji_y\right) + \underline{E}^s = e^{j\varphi}\underline{E}^i \qquad (1)$$

where i_x and i_y are the unit vector along x and y axis, respectively whereas φ represents the phase delay due to the presence of the planar TA that must assume the value 0° or 180° according to the desired phase state. From (1), the two possible scattered fields propagating along z-axis assume the following general form:

$$\underline{E}^s\left(\varphi = 0°\right) = 0$$
$$\underline{E}^s\left(\varphi = 180°\right) = -2\underline{E}^i \qquad (2)$$

By looking at (2) it can be inferred that $\underline{E}^s$ of the unit cells must be null, in case of $\varphi = 0°$, or be the double of the incident field ($\underline{E}^i$), as well as out-of-phase, in case of a desired phase delay (φ) of 180°. It is worth pointing out that the overall radiated power is the same of the incident one. To further develop the theoretical analysis, it is convenient to decompose the impinging LHCP plane wave as the sum of two orthogonal linearly polarized (LP) components as follow:

$$\underline{E}^i = \underline{E}^i_x + \underline{E}^i_y = E_0(i_x + ji_y)$$

$$\underline{E}^i_x = \frac{E_0}{2}(i_x + ji_y) + \frac{E_0}{2}(i_x - ji_y)$$

$$\underline{E}^i_y = \frac{E_0}{2}(i_x + ji_y) - \frac{E_0}{2}(i_x - ji_y) \tag{3}$$

where each LP component $\underline{E}^i_x$ and $\underline{E}^i_y$ is decomposed as the sum or the difference of two CP waves with opposite handedness. Hence, for each impinging LP component is associated to a corresponding scattered field $\underline{E}^s_x$ and $\underline{E}^s_y$.

Under the assumption that the incoming LP plane wave stimulates on the planar TA a surface current distribution capable of radiating a LHCP scattering field only along i_z axial directions, namely without back radiation, and with a phase delay of 180° with respect to the incident component, the transmitted scattered fields propagating along i_z are equal to [48]:

$$\underline{E}^{s\_LHCP}_x = \underline{E}^{s\_LHCP}_y = e^{j\pi} E_0(i_x + ji_y) \tag{4}$$

namely, the double of the LHCP component related to each incident LP EM wave shown in (3) with the addition of a 180° phase delay. Thereby, the transmitted wave ($\underline{E}^t$) turns out to be:

$$\underline{E}^t = \underline{E}^i_x + \underline{E}^i_y + \underline{E}^{s\_LHCP}_x + \underline{E}^{s\_LHCP}_y = -E_0(i_x + ji_y) \tag{5}$$

where it is visible that the transmitted wave keeps the polarization status (i.e., LHCP) with the addition of the 180° phase delay (φ) with respect to the incident field.

On the contrary, for an impinging LP wave inducing on the TA unit cells a right-handed CP (RHCP) scattered field along i_z axial direction, the transmitted scattered fields along i_z assume the following form:

$$\underline{E}^{s\_RHCP}_x = e^{j\pi} E_0(i_x - ji_y)$$

$$\underline{E}^{s\_RHCP}_y = E_0(i_x - ji_y) \tag{6}$$

namely, the double of the RHCP component related to the incident LP EM waves shown in (3) with the addition of a 180° phase delay. Thus, the transmitted wave ($\underline{E}^t$) turns out to be:

$$\underline{E}^t = \underline{E}^i_x + \underline{E}^i_y + \underline{E}^{s\_RHCP}_x + \underline{E}^{s\_RHCP}_y = E_0(i_x + ji_y) \tag{7}$$

Therefore, equations (5) and (7) prove that a structure capable of supporting unidirectional fields (i.e., along i_z) with both CP handedness, yields either 180° or 0° phase shifting by maintaining the same polarization status of the incident field and therefore turns out to be eligible to be used as 1-bit phase shifter in TA. In the following, a novel systematic design procedure based on CMA will be exploited for the synthesis of suitable TA unit cells on the basis of the scattered field guidelines derived from the described analysis.

III. CP 1-BIT PHASE SHIFTING POLARIZATION INSENSITIVE UNITCELL

The novel design procedure for the synthesis of the CP 1-bit TA unit cell relies on the CMA and it exploits the useful

insights about the scattered field of an examined object [47]. Unlike traditional TA designs, based directly on both the transmission coefficient magnitude and phase for the unit cell design of a periodic structure, an initial step for identifying the promising unit cells is carried out by exploiting the CMA. In fact, the modal analysis provides insightful guidelines to control the radiation performance of the examined object by tailoring its geometry with the aim of fulfilling the TA scattering features.

The first step of the novel approach consists of identifying two isolated scatterers capable of supporting CMs characterized by a CP radiation with an opposite handedness. Then, it is necessary to verify that the promising set of CMs radiating CP fields are efficiently stimulated by the incoming CP plane wave and that, once superimposed, they satisfy the desired characteristics on the scattered far field derived in Section II. Finally, since the CMA is performed by considering an isolated structure, the identified potential cells must be then employed as the unit cell of a periodic structure to finally assess the 1-bit unit cell performance in terms of both transmission coefficient amplitude and phase.

A. CMA OF THE ISOLATED UNIT CELL

According to the CMA, the total current distribution on an object can be decomposed as a weighted linear superposition of orthogonal current modes (J_n) [49], [50], [51]. The inspection of the modal analysis and the related far fields provide meaningful insight of the scattering and radiation proprieties of a structure, based only on its geometry and regardless of the feeding arrangement [52], [53]. Therefore, the CMA provides helpful design guidelines to control the radiation performance of the examined object by tailoring its geometry.

The potential candidate transmitting unit cells (i.e., cell-0 and cell-1) to be employed in the CP 1-bit TA belong to the class of cells supporting a CP scattered field presented in [48]. As shown in Fig. 1 each of them comprises two metallic layers, connected through vias with a diameter of 0.3 mm realizing four tight three dimensional (3D) meandered dipoles arranged with a fourfold rotational symmetry. This feature allows achieving the polarization insensitive characteristic as well as to improve its frequency response robustness with respect to the oblique incidence [54]. Specifically, cell-1 (Fig. 1b) is derived from cell-0 (Fig. 1a) by swapping the top and bottom metallic layers.

The modal behavior of the structures in Fig. 1 is then investigated to reveal their field radiated. The eigenvalues (λ_n) of the first five CMs as a function of the frequency are shown in Fig. 2. It can be drawn that, within the addressed frequency band, just the first three CMs could give a significant contribution to the scattered field, since they resonate (i.e., $\lambda_n = 0$) within the considered frequency range. More in detail, the 3D unit cells support two degenerate modes (i.e., Mode#1 and Mode#2) with a resonance frequency of 8 GHz and a high-quality factor mode (i.e., Mode#3) with a resonance frequency close to 7.55 GHz whereas Mode#4
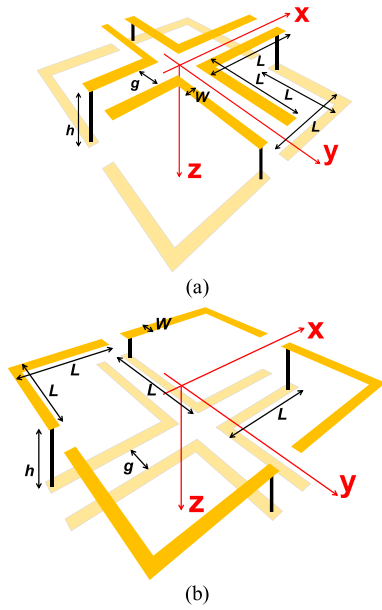
FIGURE 1. Meandered dipoles with a fourfold rotational symmetry layout: L = 3.94 mm, W = 0.65 mm, g = 0.4 mm and h = 4.3 mm; (a) cell-0 and (b) cell-1.

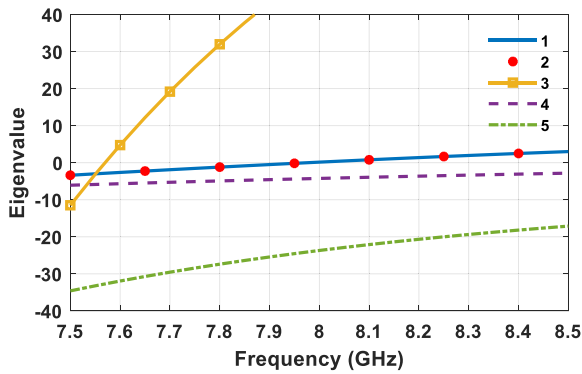**FIGURE 2.** Eigenvalues as a function of the frequency of the 3D structure with a fourfold rotational symmetry.

FIGURE 3. Normalized current distributions (left column) and normalized scattering field (right column) related to (a) Mode#1@8 GHz, (b) Mode#2@8 GHz and (c) Mode#3@7.55 GHz.

FIGURE 4. Normalized scattered field in dB related to Mode#1 and Mode#2 as a function of the θ angle evaluated at 8 GHz for $\varphi = 90°$; (a) cell-0, (b) cell-1.

and Mode#5 are identified as higher order capacitive modes ($\lambda_n < 0$) since their resonance is above 8.5 GHz. Particularly, the length of the employed meandered dipoles turns out to be 0.5 λ where λ represents the wavelength at the resonance frequency of degenerate modes (*i.e.*, 8 GHz).

Fig. 3 shows the modal current distribution and the 3D normalized radiation patterns of the first three CMs.

More in detail, degenerate modes exhibit a modal current mainly distributed along two of the four meandered dipoles capable of radiating a scattered field with maximum values along $\theta = 0°$ and $\theta = 180°$ (*i.e.*, i_z and $-i_z$) as depicted in Fig. 3a-b. On the contrary, Mode#3 provides a modal radiation pattern with a pattern null along broadside direction ($\theta = 0°$) and with four peaks toward $\theta = 90°$ due to a major current distribution over the entire structure (Fig. 3c). Therefore, the set of CMs that could satisfy the derived scattered field requirements to realize a CP 1-bit TA comprises only the two degenerate modes.
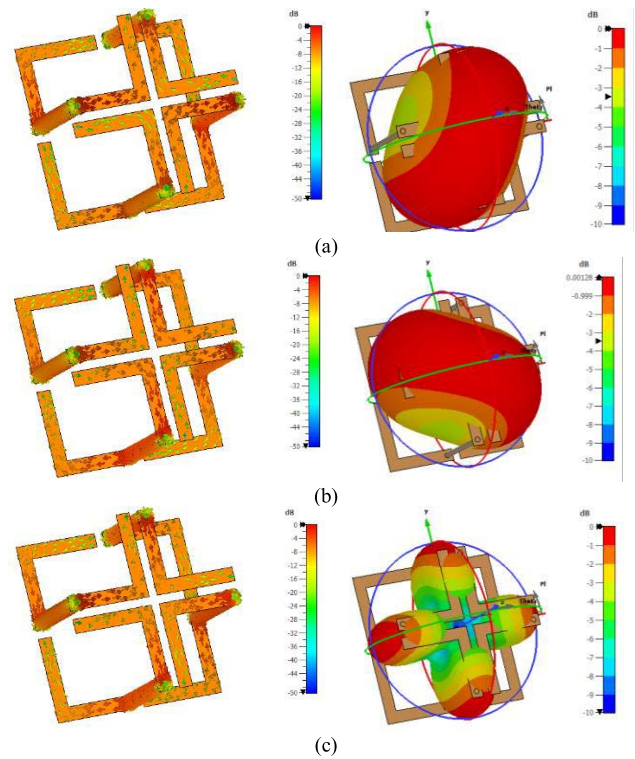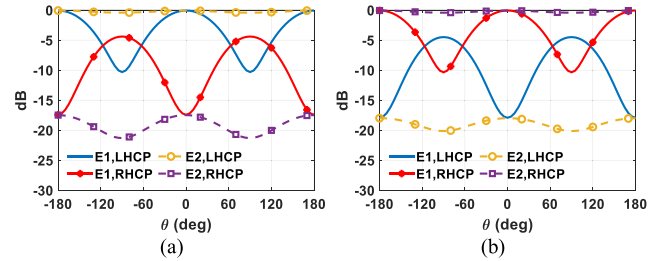
The normalized scattered fields for both Mode#1 and Mode#2 are shown in Fig. 4 as a function of the θ angle in a principal plane ($\varphi = 90°$) to identify their modal field polarization.

From Fig. 4 it is evident that the degenerate modes for cell-0 and cell-1 are characterized by a bidirectional radiation pattern with a circular polarization. Specifically, the couple of modes related to cell-0 radiate mainly a LHCP along $\theta = 0°$ and $\theta = 180°$ (*E1,LHCP* and *E2,LHCP*) with a cross polar component below -17 dB (Fig. 4a). Conversely, the opposite CP sense, namely a RHCP (*E1,RHCP* and *E2,RHCP*), is provided by swapping the metallic layers (Fig. 4b).

It is worth pointing out that, although the pair of degenerate modes for both the cell-0 and cell-1 are characterized by a circular polarization, each CM provides a
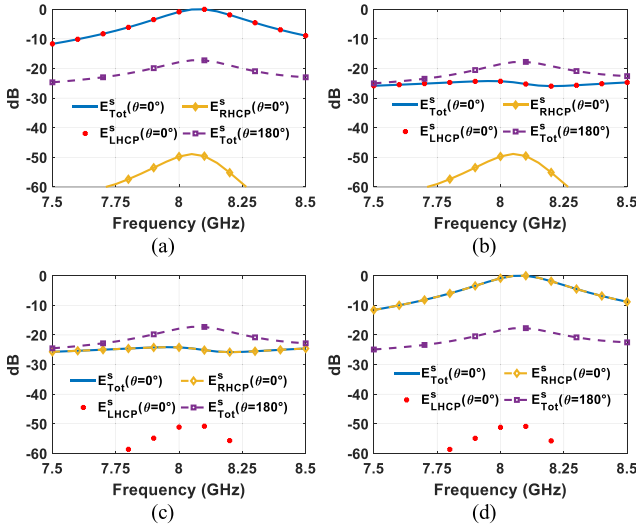
FIGURE 5. Normalized scattering field (E^s) as a function of the frequency for cell-0 (left column) and cell-1 (right column) structure in case of a normally impinging (a)-(b) LHCP plane wave and (c)-(d) RHCP.
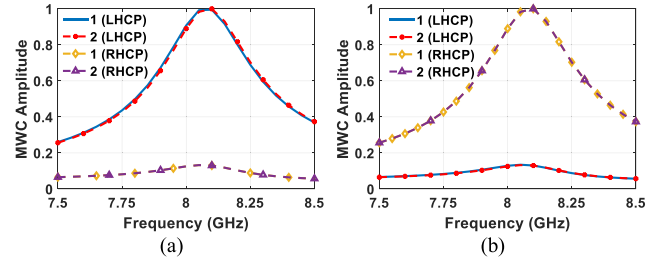

FIGURE 6. MWC amplitude as a function of the frequency by considering both the RHCP and LHCP normally impinging plane wave; (a) cell-0 and (b) cell-1.

bidirectional radiation pattern (Fig. 3) and hence cannot meet the unidirectional radiation constraint derived in Section II. Hence, it is necessary to understand if a suitable CMs excitation can lead to a backscattering suppression. To this aim, the normalized scattered field (E^s) as a function of the frequency for cell-0 and cell-1 under the illumination of either normally impinging LHCP or RHCP plane wave is investigated. By looking at Fig. 5 it can be inferred that, in case of a normally impinging CP plane wave propagating along z-axis, both the investigated platforms guarantee either a CP transmitted scattered field with a strong back scattering reduction or a negligible scattered field value, meeting the derived CP 1-bit TA scattered field (E^s) conditions of Section II. More in detail, by considering a LHCP incident wave, cell-0 (Fig. 5a) provides a robust scattered field with the same polarization ($E^s_{LHCP}(0°)$) with a maximum value around the degenerate modes resonance frequency of 8 GHz, whereas the cell-1 (Fig. 5b), turns out to be almost transparent since its normalized scattered field is around 25 dB lower than the maximum scattering of cell-0. The same scattering field behavior occurs in case of a RHCP incident wave (Fig. 5c-d) but with an exchange of the sensitive cell to the incoming plane wave, namely cell-1 instead of cell-0. The frequency selectivity depends on the supported CMs of the structure as previously shown in the modal scattered field (Fig. 4).

The forward scattering field guaranteed by the investigated cells is due to the efficient modal excitation of both Mode#1 and Mode#2, as depicted by the modal weighting coefficient (MWC) amplitude [55] reported in Fig. 6. In fact, for cell-0 in case of an impinging LHCP plane wave, nearby both the Mode#1 and Mode#2 resonance, namely 8 GHz, the CP CMs reach the maximum stimulation on the platform (Fig. 6a). This pivotal feature, necessary for obtaining a phase delay (φ) of 180° as will be shown in the following sub-section,

occurs since the couple of excited CMs has a MWC phase difference close to 90° within the investigated frequency band. Conversely, when a RHCP plane wave impinges on cell-0 (Fig. 6a) the modal excitation degree of degenerate modes is considerable reduced since they support mainly an opposite CP handedness (Fig. 4b). It is worth noting that the other CMs are not stimulated since they are characterized by a modest MS value or a pattern null toward broadside. The same behavior can be observed with cell-1 but exchanging the LHCP and RHCP MWC response as visible in Fig. 6b.

The described scattered field behavior, for both the cell-0 and cell-1 with respect to the incoming CP plane wave sense, is at the basis of the CP property of the proposed CP 1-bit TA. Therefore, CMA emphasized in a very effective way that the 3D meandered dipoles with fourfold rotational symmetry satisfies the necessary scattering field requirements thanks to the pair of CP CMs. In particular, by exchanging the metallic layers it is possible to alter the CP CMs handedness necessary to provide 180° or 0° phase state as shown in (5) and (7). Hence it can be suitably adopted as the unit cell of a periodic structure to realize a 1-bit phase shifter in TA.

B. PERIODIC STRUCTURE PERFORMANCE ASSESSMENT

With the aim of assessing the dual-layer-based CP 1-bit phase shifting, the platform individuated by the help of CMA has been employed as the unit cell of a periodic structure. The full-wave simulation has been carried out with CST Microwave Studio by setting a periodicity equal to 9.2 mm, namely around $0.24 \lambda_{@8 \text{ GHz}}$. In fact, it is favorable to keep it as small as possible for avoiding the rise of grating lobes as well as to reduce the frequency response sensitivity of the unit cell in the event of oblique incidence [56].

The frequency response in terms of copolar (T_{co}) and cross polar (T_{cros}) transmission coefficient magnitude in case of a LHCP incoming plane wave by considering various incidence angles (θ_i) in the range $0° - 45°$ is shown in Fig. 7.

Fig. 7 highlights that both investigated cells (i.e., cell-0 and cell-1) exhibit almost identical performance by behaving like an all-pass filter within the addressed frequency. Indeed, the copolar transmission coefficient (T_{co}) turns out to be superior to -1.3 dB for the whole examined frequency range whereas at 8 GHz remains better to -0.49 dB. It is
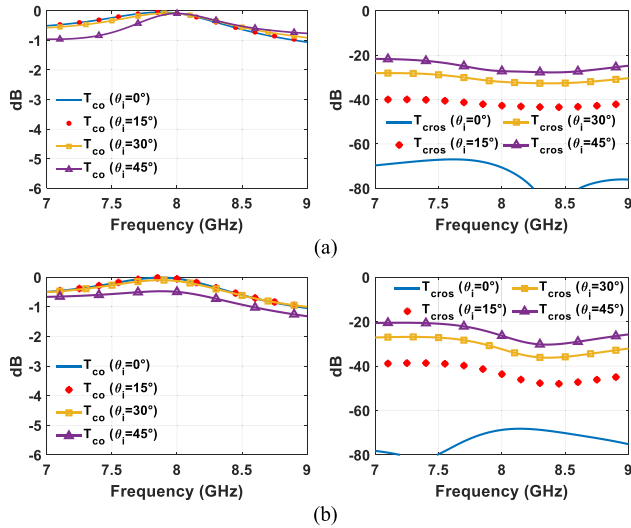
FIGURE 7. Copolar (T_{co}) and cross polar (T_{cros}) transmission coefficient amplitude in dB as a function of the frequency for different incidence angles (θ_i) by considering a LHCP impinging wave; (a) cell-0 and (b) cell-1.

FIGURE 8. (a) Copolar transmission coefficient phase and (b) phase difference between cell-0 (T^0) and cell-1 (T^1) as a function of the frequency for different incidence angles (θ_i) by considering a LHCP impinging wave.

noteworthy to observe that the highest T_{co} occurs close to 8 GHz, namely at the resonance frequency of the supported couple of CP CMs (Fig. 2). Hence, the periodic setting does not alter the frequency response of the platform retrieved by the help of CMA. Then, cell-0 guarantees a forward CP scattered field (Fig. 5a) whereas a negligible scattered field value occurs in case of cell-1 (Fig. 5b) since it supports an opposite CP CMs handedness then the incoming LHCP plane wave. Besides, the cross-polar transmission coefficient (T_{cros}) is maintained below -20 dB for the whole addressed frequencies and incidence angles (θ_i) by emphasizing a prominent polarization purity of the transmitted LHCP wave.

Fig. 8a shows the copolar transmission coefficient phase related to cell-0 (T^0) and cell-1 (T^1). It can be asserted that, the impinging LHCP plane wave undergoes a sharp phase delay included from $-100°$ to $-350°$ within the frequency range 7 GHz – 9 GHz in case of cell-0. On the contrary, by employing a cell-1-based periodic structure the transmission phase undertakes a softer variation as a function of the frequency. Moreover, since all the transmission coefficient phase curves related to T^0 and T^1 are largely overlapped, the investigated unit cells provide a remarkable robustness to oblique incidence, pivotal feature for a TA. The different transmission phase behavior is due to the excitation or not on the periodic structure of the supported degenerate CP CMs previously identified as Mode#1 and Mode#2. Precisely, the impinging LHCP plane wave on the cell-0-based periodic structure efficiently stimulates the supported LHCP CMs (Fig. 4a), whereas it passes almost unchanged in case of cell-1 since it supports RHCP CMs (Fig. 4b) as accurately predicted by the CMA. This phase trend leads to a copolar transmission coefficient phase difference between cell-0 and cell-1 (Fig. 8b) that decrease little by little with the increase of frequency by reaching around $-180°$ at 8 GHz. Both the transmission coefficient amplitude (Fig. 7) and phase
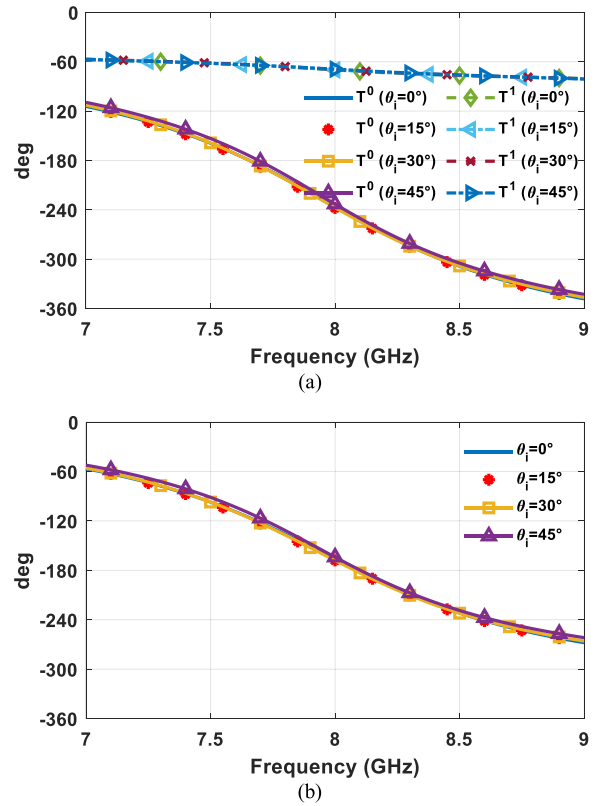
(Fig. 8) validate the scattered field guidelines derived in Section II as well as the previous CMA by pointing out that the mutual coupling effect among nearby unit cells in the considered array structures is not significant. Moreover, they confirm the suitability of the proposed two unit cells to be employed in a CP 1-bit TA.

However, it is worth observing that, in general, once the supported CMs of an isolated platform are known, it is easier to cope with some possible performance alterations due to the coupling of nearby cells. Indeed, the inspection of the modal distribution could provide valuable insights and guidelines to tackle the unwanted performance deterioration of the periodic structure. This represents another notable advantage of the CMA approach instead of a the traditional one that turns out to be lacking in physical insights.

It is worth noting that, a frequency shift of the supported degenerate CP CMs can be obtained by scaling the transmitting unit cells that could be then exploited for achieving a multi-bit spatial phase shifter TA.

IV. CP 1-BIT TA DESIGN
All the previous considerations provided the necessary building blocks to realize the novel CMA-inspired CP 1-bit TA by exploiting a miniaturized dual-layer polarization-insensitive transmitting unit cells. To validate the concept, the CP 1-bit dual-layer TA has been etched on a dielectric

substrate layer (ISOLA IS680-280, $\varepsilon_r = 2.8$, $\tan\delta = 0.0025$) with a thickness of 3.04 mm. The converter geometrical dimensions have been slightly adjusted from Section III due to the presence of the dielectric layer, thus leading to an FSS periodicity equal to 6.67 mm. The whole TA panel is then illuminated by an ideal LHCP point-source acting as the primary feeder, with a radiation pattern equal to that of a horn antenna (MVG QR2000, 2–18 GHz) characterized by a gain of 15 dBi at 8 GHz, placed at a particular distance from the TA structure, known as the focal point. The phase profile on the TA panel of the primary feeder incident wave was used for the selection of the TA unit cell types (*i.e.*, cell-0 or cell-1) to collimate the beam at broadside direction ($\theta = 0°$) according to the following rule:

$$270° < \phi^i(n, m, f_0) \leq 90° \rightarrow \phi^{cell}(n, m) = T^1$$
$$90° < \phi^i(n, m, f_0) \leq 270° \rightarrow \phi^{cell}(n, m) = T^0 \quad (8)$$

where $\phi^i(n, m, f_0)$ represents the impinging electromagnetic wave phase on the $(n,m)^{th}$ unit cell evaluated at the reference frequency f_0 whereas $\phi^{cell}(n,m)$ is the additional phase contribution to the scattered field of the $(n,m)^{th}$ unit cell. Hence, if the impinging electromagnetic wave phase at the reference frequency f_0 is smaller than 90° or larger than 270°, the unit cell that provide a negligible copolar transmission coefficient phase (cell-1) in case of a LHCP impinging wave is applied. On the contrary, the unit cell with a copolar phase difference transmission coefficient phase of 180° (cell-0) is employed.

To calculate the TA radiation patterns in the far field, a hybrid approach involving both full-wave simulations and numerical calculations in MATLAB have been considered. Precisely, the employed unit cells were simulated separately using periodic boundary conditions as previously explained in Section III for both transmission amplitude and phase response related to each TA element. Indeed, they depend on the frequency, the impinging wave incidence angle (θ_i) and polarization. Then, each TA cell is considered as an individual radiator with its corresponding amplitude and phase, and a MATLAB code has been implemented according to the phased array theory.

By considering a TA panel comprising 43×30 elements with an aperture area equal to 287×200 mm^2 the impact of the position of the employed horn antenna on the TA gain toward broadside direction ($\theta = 0°$) has been investigated by assuming different focal point to maximum TA dimension ratio (F/D) and a reference frequency for the TA panel construction equal to $f_0 = 8$ GHz. From Fig. 9 it can be asserted that the TA gain reaches a maximum value around 8.1 GHz and then it tends to go down with the increasing of the frequency with dissimilar slope according to the employed F/D value.

This happens because the unit cells present a maximum copolar transmission coefficient amplitude (Fig. 7) along with a copolar transmission coefficient phase difference between cells-0 and cell-1 of around 180° (Fig. 8b) nearby
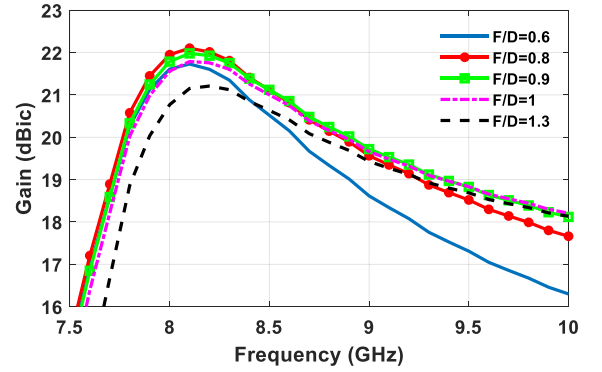

FIGURE 9. Calculated TA gain toward $\theta = 0°$ as a function of the frequency for different F/D values.

8 GHz. In general, large F/D values lead to a wider 3 dB gain bandwidth ($BW_{3\ dB}$) owing to the lower and lower electrically distances among TA elements and the primary feeder. Nevertheless, it determines a reduction of the maximum gain due to a worse primary feeder spillover efficiency. Therefore, with the increasing of the F/D value it is necessary to employ more directive primary feeders capable to reduce the spillover loss and so guarantee a TA gain enhancement [21]. However, the rise of the F/D value leads to bulky antenna structures, making them not compliant to many systems that require low profile designs.

An F/D value equal to 0.8, that corresponds to a distance between the TA panel and the adopted horn antenna equal to 229 mm, has been selected for achieving the highest TA gain equal to 22.1 dBic at 8.1 GHz. In such case, the resultant 1 dB gain percentage bandwidth ($BW_{1\ dB}$) and 3 dB gain percentage bandwidth ($BW_{3\ dB}$) turn out to be 7.95 % (7.85 GHz - 8.5 GHz) and 17.5 % (7.72 GHz - 9.2 GHz), respectively.

The color map highlighting the TA unit cell types (*i.e.*, cell-0 or cell-1) to collimate the beam at broadside direction ($\theta = 0°$) retrieved at the reference frequency $f_0 = 8$ GHz is illustrated in Fig. 10 with two different colors (*i.e.*, blue color for cell-1 whereas yellow one for the cell-0 configuration). Fig. 11 displays the normalized radiation pattern in the principal planes ($\phi = 0°$ and $\phi = 90°$) at the frequency of 7.72 GHz, 8.1 GHz and 9.2 GHz.

As it can be inferred from the calculated radiation patterns of Fig. 11 the designed CP 1-bit TA produces high-gain pencil beams in the broadside direction with reasonable low lateral lobes. More in detail, at the extremes of the $BW_{3\ dB}$, namely 7.72 GHz and 9.2 GHz, the peak side lobe level (PSLL) turns out to be – 9.5 dB and −10.7 dB respectively, whereas at 8.1 GHz it reaches – 17 dB. The rise of lateral lobes at the extremes of the $BW_{3\ dB}$ is due to a beamforming degradation due to a suboptimal phase profile of the TA panel, similar to what happens in phased arrays in case of radiating elements feeding unbalance [14].

As a further distinguish feature, the calculated cross-polarization discrimination (XPD) of the proposed TA turns
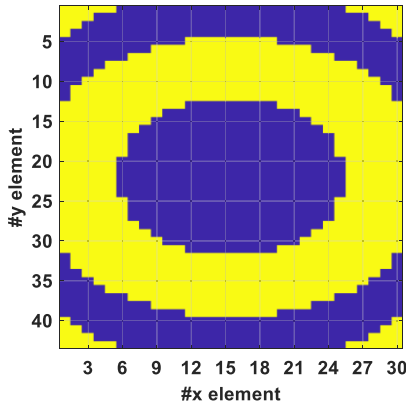
FIGURE 10. Color map highlighting the arrangement of the two unit cells populating the CP 1-bit TA panel evaluated at 8 GHz in case of a F/D = 0.8; blue color for cell-1 whereas yellow one for the cell-0 configuration.
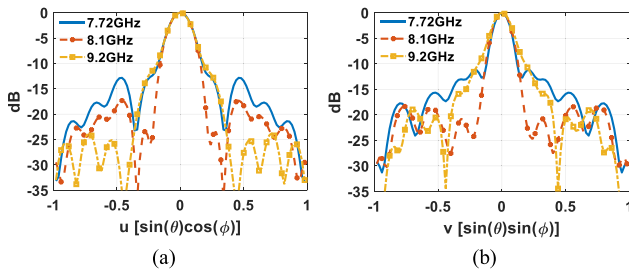

FIGURE 11. Calculated normalized radiation pattern in dB for three different frequencies; (a) $\phi = 0°$ and (b) $\phi = 90°$.

FIGURE 12. CP 1-bit TA manufactured prototype. The inset highlights the discretization along the two-phase border.

FIGURE 13. Measured S_{11} in dB as a function of the frequency of the employed horn antenna in free space (void) and with the manufactured TA panel.

FIGURE 14. Comparison between the calculated and measured TA gain as a function of the frequency when the TA panel is illuminated by a LHCP horn primary feeder.

out to be higher than 40 dB without applying any phase compensation scheme [39], meaning that the TA XPD is basically determined by the employed primary feeder. This is accomplished thanks to the remarkable polarization purity of the employed unit cells (Fig. 7) capable to support a couple of CP CMs.

V. PROTOTYPE AND MEASUREMENTS

A miniaturized dual-layer polarization-insensitive TA comprising 43×30 unit cells etched on a ISOLA IS680-280 substrate layer with a thickness of 3.04 mm has been manufactured to assess the reliability of the proposed approach. The whole TA panel and a zoomed-in view of a few unit cells are shown in Fig. 12. The TA panel shown in Fig. 12 is illuminated with a dual-polarized horn antennas (MVG QR2000, 2 - 18 GHz) placed at a F/D = 0.8. Then, the transmitted field is collected by another dual-polarized horn antennas (MVG QR2000, 2 - 18 GHz) placed at around 2 m with respect to the TA panel.

The horn antennas are connected to a four ports vector network analyzer (Anritsu Shockline MS46524B). To produce a LHCP wave, the two horn antenna ports of the primary feeder were combined in post processing. The measured reflection coefficient (S_{11}) in dB of the employed horn antenna with and without the designed TA panel is reposted in Fig. 13.
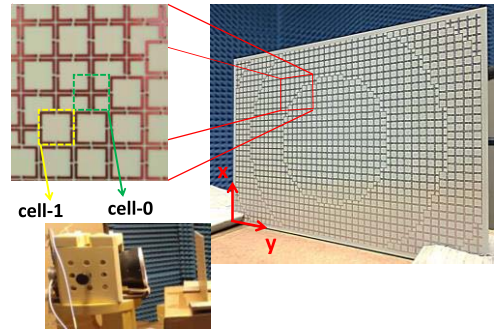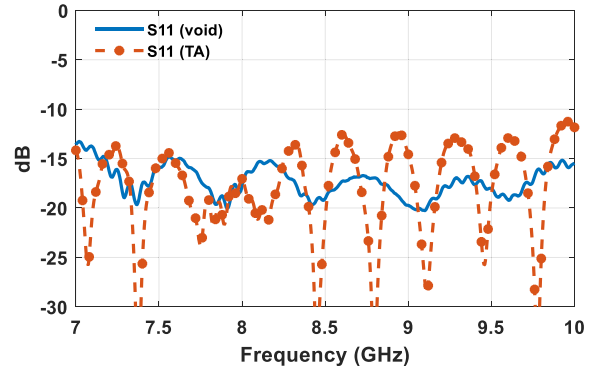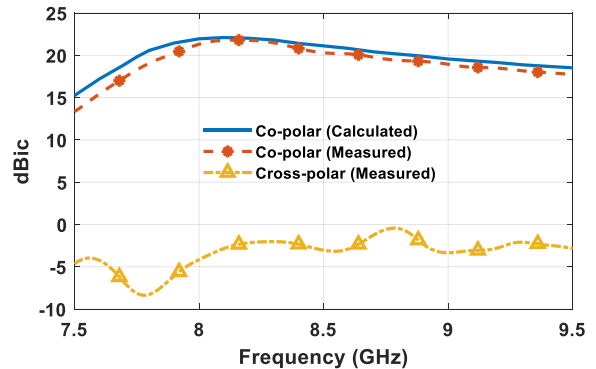
The small S_{11} alterations of the employed primary feeder underlines that most of the spherical wave that impinges on the TA panel is transmitted and not reflected.

The comparison between the calculated and measured TA gain toward broadside direction ($\theta = 0°$) is reported in Fig. 14.

The manufactured CP 1-bit TA presents a percentage $BW_{1\ dB}$ and $BW_{3\ dB}$ of 5.63 % (7.94 GHz - 8.4 GHz) and 15.22 % (7.77 GHz - 9.05 GHz), respectively, with a maximum gain value equal to 21.8 dBic at 8.14 GHz instead of a predicted value of 22.1 dBic (Fig. 9). Small
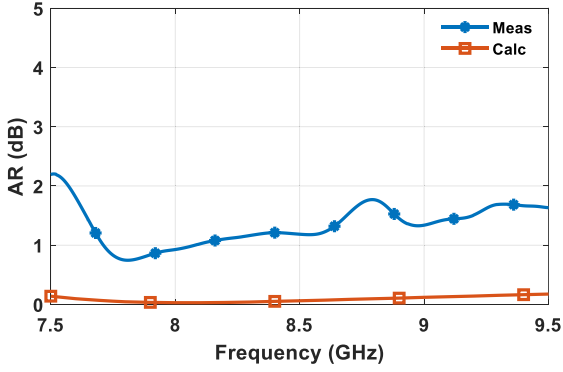
FIGURE 15. Comparison between measured and calculated TA axial ratio (AR) as a function of the frequency when the TA panel is illuminated by a LHCP horn primary feeder.
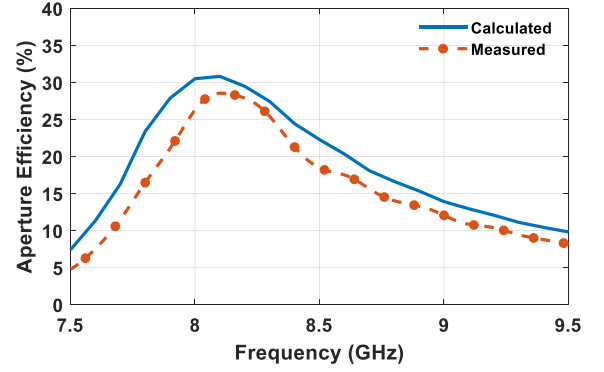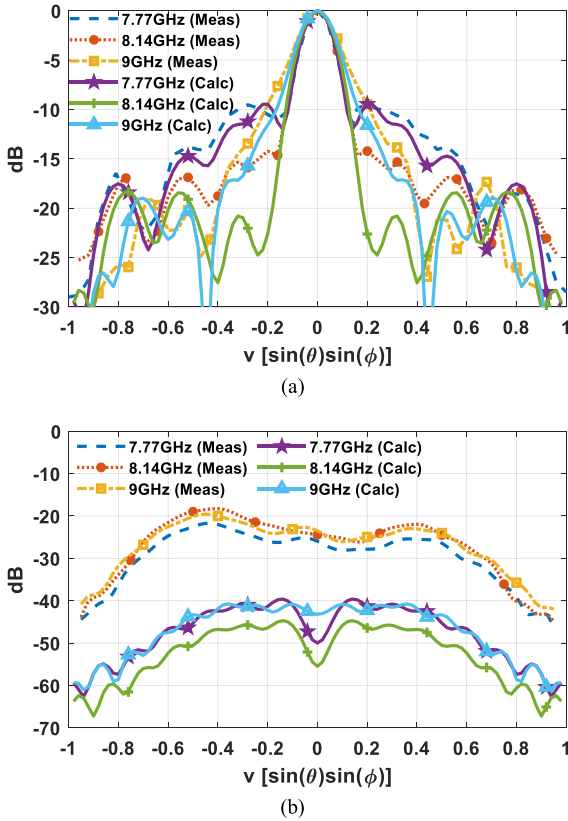

(a)

(b)

FIGURE 16. Comparison between measured and calculated (a) copolar and (b) cross-polar normalized radiation pattern in dB for three different frequencies at $\phi = 90°$ plane.

discrepancies can be ascribed to the fabrication tolerances as well as mild variations of the dielectric material with respect to the situated one.

The measured cross-polar value at broadside ($\theta = 0°$) turns out to be at least 20 dB lower than the copolar one within the $BW_{3\ dB}$ thus guarantying an axial ratio (AR) value lower than 1.75 dB and, in general, lower than 2 dB within the addressed frequency range (Fig. 15).

This fact further confirms the remarkable polarization purity of the CMA-inspired TA panel as stated in Section III.

FIGURE 17. Comparison between the calculated and measured aperture efficiency (η_{ap}) as a function of the frequency when the TA panel is illuminated by a LHCP horn primary feeder.

TABLE 1. Detailed calculated CP TA efficiencies at 8.14 GHz.

Efficiency		%	dB
Primary feeder	Spillover	85	−0.7
	Illumination	88	−0.55
Phase scheme	Ideal 1-Bit	46	−3.37
TA panel	Phase	98.5	−0.06
	Transmission	91	−0.4
	Aperture	30.8	−5.08

In fact, cross-polar component is mainly determined by the employed primary feeder.

By considering a central frequency of 8.4 GHz, the proposed CP 1-bit TA panel has a thin thickness equal to $0.085\ \lambda_{@8.4\ GHz}$ with an inter elements distance of around $0.19\ \lambda_{@8.4\ GHz}$.

Fig. 16 shows the comparison between the calculated and measured copolar and cross-polar normalized radiation pattern for different frequencies within the $BW_{3\ dB}$. The measured copolar results confirm that the proposed CP 1-bit TA produces a pencil beam at broadside ($\theta = 0°$) with a satisfactory agreement with respect to the calculated ones. As above mentioned, the measured cross-polar rise with respect to the calculated one is due to the employed primary feeder, not to the TA panel.

In addition, both the calculated aperture efficiency (η_{ap_calc}) and the measured one (η_{ap_meas}), obtained by the ratio between the TA gain and the directivity of an aperture, with the same TA geometrical dimensions and an effective area equal to the geometrical one, have been depicted in Fig. 17. Specifically, the formula exploited for both the calculated and measured aperture efficiencies ($\eta_{ap\_calc/meas}$) assessment is equal to:

$$\eta_{ap\_cal/meas} = \frac{G_{calc/meas}(\theta = 0°)}{\frac{4\pi}{\lambda^2} A_{geo}} \quad (9)$$

where the numerator represents the calculated or measured TA gain at broadside direction ($\theta = 0°$) whereas the denominator is the ideal directivity of an aperture with the

TABLE 2. Measured performance comparison among different CP TA.

Ref	Frequency (GHz)	Metallic Layers	Phase Coverage	Unit-Cell Dimension (λ^2)	Thickness (λ)	BW_{-1dB}/BW_{-3dB} (%)	Peak Aperture Efficiency (%)	F/D
[43]	27	6	3-bit	0.5×0.5	0.66	22/47	17	1
[42]	20	3	3-bit	0.5×0.5	0.14	15.2/N.R.	60.2	1
[44]	30	3	3-bit	0.5×0.5	0.1	9.2/15.9	51.2	0.67
[46]	30	3	1-bit	0.5×0.5	0.11	9.5/20	15.1	0.52
[33]	20	2	360°	0.47×0.47	0.2	9.5/N.R.	60	1
[35]	14	2	360°	0.32×0.32	0.075	3.5/8.5	41	0.4
This work	8.4	2	1-bit	0.19×0.19	0.085	5.63/15.22	28.5	0.8

same dimensions of the TA with an effective area equal to the geometrical area (A_{geo}).

The maximum measured aperture efficiency of the CP TA antenna is 28.5 % at 8.14 GHz which is slightly lower than the calculated one (30.8 %).

It is worth noting that the aperture efficiency is the result of a combination of different factors. Indeed, the maximum reachable aperture efficiency (η_{ap_MAX}) turns out to be 34% by considering the employed horn primary feeder (MVG QR2000), F/D = 0.8 and an ideal 1-bit scheme, namely all cells transmission amplitude equal to 1 with ideal phases of 0° or 180°, This means that the aperture efficiency is slightly deteriorated due to the presence of the TA panel. Therefore, the calculated and measured estimated TA radiation efficiency (η_{rad}), namely the ratio between the peak η_{ap_calc} or η_{ap_meas} and η_{ap_MAX}, appears to be 90 % and 84 %, respectively, thus confirming the unit cell's high efficiency. It is worth observing that the more the radiation pattern model of the primary feeder approximates the real one, the better is the efficiencies estimation.

The different calculated efficiencies of the CP TA evaluated at 8.14 GHz are presented in Table 1. The phase scheme efficiency, based on two ideal phase states only, is found to be the dominant factor (-3.37 dB) on the total calculated CP TA aperture efficiency of 30.8 % (-5.08 dB). The employed primarily feeder and the selected F/D = 0.8 determine an overall efficiency of around 75 % (*i.e.*, 85 % for the spillover efficiency and 88 % for the illumination one) whereas the TA panel, in terms of both phase and transmission efficiency, have a negligible impact on the total TA efficiency budget, by providing an overall loss of 0.46 dB (*i.e.*, overall efficiency of around 90 %), thus confirming the unit cell's high efficiency.

To highlight the noteworthy performance of the proposed CMA-based CP 1-bit TA a comparison with respect to the previously proposed CP TAs is summarized in Table 2. Compared to the previously reported phase quantized-based CP TAs, the proposed CMA-inspired design is characterized by the lowest TA thickness (0.085 λ_0) and it is the only one that uses two metallic layers. Note that the thinnest CP TA profile feature is also preserved by considering the continuous phase CP TAs, except [35]. However, even

though [35] presents a slightly lower profile, the proposed TA offers about the double gain percentage bandwidth.

Therefore, the proposed novel approach for designing a CP 1-bit TA by resorting to the CMA provides low profile and an easy-to-fabricate solution with interesting radiative performance. It is worth mentioning that this is the first time that CMA has been employed for the design of a CP TA. In fact, although the TAs proposed in [57], [58] exploit the modal analysis, they refer to a linearly polarized (LP) antenna and for a not-quantized phase resolution.

VI. CONCLUSION

A novel CP 1-bit dual-layer TA has been proposed by resorting to the CMA-inspired theoretical study. After the theoretical analysis concerning the TA scattered field ($\underline{E}^s$) required conditions, design guidelines for identifying two unit cells capable of supporting CMs radiating either RHCP or LHCP scattered field are provided on the basis of useful insights offered by the CM theory. The proposed CP 1-bit TA stands out for the lowest TA thickness (0.085 $\lambda_{@8.4\ GHz}$) as well as for the use of two metallic layers only, thus reducing the fabrication complexity. The efficient modal excitation on the employed unit cells of a couple of CMs radiating either RHCP or LHCP scattered field guarantees both a low copolar IL as well as a copolar transmission phase difference of 0° or 180°. The results showed a remarkable TA radiative performance able to provide a meaningful working bandwidth and, at the same time, offering the most compact design. Measurements on a realized prototype are in a good agreement with simulations, confirming the reliability and the applicability of the proposed theoretical approach. Furthermore, both the smallest unit cell periodicity as well as the high η_{rad} help to attain an appreciable peak of the aperture efficiency, even with the adoption of a 1-bit phase coverage.

REFERENCES

[1] Y. J. Guo, M. Ansari, R. W. Ziolkowski, and N. J. G. Fonseca, "Quasi-optical multi-beam antenna technologies for B5G and 6G mmWave and THz networks: A review," *IEEE Open J. Antennas Propag.*, vol. 2, pp. 807–830, 2021, doi: 10.1109/OJAP.2021.3093622.

[2] W. Jiang, B. Han, M. A. Habibi, and H. D. Schotten, "The road towards 6G: A comprehensive survey," *IEEE Open J. Commun. Soc.*, vol. 2, pp. 334–366, 2021, doi: 10.1109/OJCOMS.2021.3057679.

[3] F. A. Dicandia and S. Genovesi, "Exploitation of triangular lattice arrays for improved spectral efficiency in massive MIMO 5G systems," *IEEE Access*, vol. 9, pp. 17530–17543, 2021, doi: 10.1109/ACCESS.2021.3053091.

[4] R. Flamini et al., "Towards a heterogeneous smart electromagnetic environment for millimeter-wave communications: An industrial viewpoint," *IEEE Trans. Antennas Propag.*, vol. 70, no. 10, pp. 8898–8910, Oct. 2022, doi: 10.1109/TAP.2022.3151978.

[5] F. A. Dicandia, N. J. G. Fonseca, M. Bacco, S. Mugnaini, and S. Genovesi, "Space-air-ground integrated 6G wireless communication networks: A review of antenna technologies and application scenarios," *Sensors*, vol. 22, no. 9, p. 3136, Apr. 2022, doi: 10.3390/s22093136.

[6] S. Genovesi, F. Costa, F. A. Dicandia, M. Borgese, and G. Manara, "Orientation-insensitive and normalization-free reading chipless RFID system based on circular polarization interrogation," *IEEE Trans. Antennas Propag.*, vol. 68, no. 3, pp. 2370–2378, Mar. 2020, doi: 10.1109/TAP.2019.2949417.

[7] S. Genovesi and F. A. Dicandia, "Characteristic modes analysis of a near-field polarization-conversion metasurface for the design of a wideband circularly polarized X-band antenna," *IEEE Access*, vol. 10, pp. 88932–88940, 2022, doi: 10.1109/ACCESS.2022.3200303.

[8] S. S. Gao, Q. Luo, and F. Zhu, *Circularly Polarized Antennas*. Hoboken, NJ, USA: Wiley, 2013.

[9] M. Giordani and M. Zorzi, "Non-terrestrial networks in the 6G era: Challenges and opportunities," *IEEE Netw.*, vol. 35, no. 2, pp. 244–251, Mar./Apr. 2021, doi: 10.1109/MNET.011.2000493.

[10] F. A. Dicandia and S. Genovesi, "Spectral efficiency improvement of 5G massive mimo systems for high-altitude platform stations by using triangular lattice arrays," *Sensors*, vol. 21, no. 9, p. 3202, May 2021, doi: 10.3390/s21093202.

[11] A. H. Aljuhani, T. Kanar, S. Zihir, and G. M. Rebeiz, "A 256-element ku-band polarization agile satcom receive phased array with wide-angle scanning and high polarization purity," *IEEE Trans. Microw. Theory Techn.*, vol. 69, no. 5, pp. 2609–2628, May 2021, doi: 10.1109/TMTT.2021.3056439.

[12] X. Gu et al., "Development, implementation, and characterization of a 64-element dual-polarized phased-array antenna module for 28-GHz high-speed data communications," *IEEE Trans. Microw. Theory Techn.*, vol. 67, no. 7, pp. 2975–2984, Jul. 2019, doi: 10.1109/TMTT.2019.2912819.

[13] P. Rocca, G. Oliveri, R. J. Mailloux, and A. Massa, "Unconventional phased array architectures and design methodologies—A review," *Proc. IEEE*, vol. 104, no. 3, pp. 544–560, Mar. 2016, doi: 10.1109/JPROC.2015.2512389.

[14] F. A. Dicandia and S. Genovesi, "Wide-scan and energy-saving phased arrays by exploiting penrose tiling subarrays," *IEEE Trans. Antennas Propag.*, vol. 70, no. 9, pp. 7524–7537, Sep. 2022, doi: 10.1109/TAP.2022.3178917.

[15] J. R. Reis, M. Vala, and R. F. S. Caldeirinha, "Review paper on transmitarray antennas," *IEEE Access*, vol. 7, pp. 94171–94188, 2019, doi: 10.1109/ACCESS.2019.2924293.

[16] O. Orgeira, G. León, N. J. G. Fonseca, P. Mongelos, and O. Quevedo-Teruel, "Near-field focusing multibeam geodesic lens antenna for stable aggregate gain in far-field," *IEEE Trans. Antennas Propag.*, vol. 70, no. 5, pp. 3320–3328, May 2022, doi: 10.1109/TAP.2021.3139093.

[17] O. Quevedo-Teruel et al., "Geodesic lens antennas for 5G and beyond," *IEEE Commun. Mag.*, vol. 60, no. 1, pp. 40–45, Jan. 2022, doi: 10.1109/MCOM.001.2100545.

[18] L.-Z. Song, P.-Y. Qin, and Y. J. Guo, "A high-efficiency conformal transmitarray antenna employing dual-layer ultrathin huygens element," *IEEE Trans. Antennas Propag.*, vol. 69, no. 2, pp. 848–858, Feb. 2021, doi: 10.1109/TAP.2020.3016157.

[19] M. J. Veljovic and A. K. Skrivervik, "Circularly polarized transmitarray antenna for cubesat intersatellite links in K-band," *IEEE Antennas Wireless Propag. Lett.*, vol. 19, no. 10, pp. 1749–1753, Oct. 2020, doi: 10.1109/LAWP.2020.3016340.

[20] H. Hasani, J. S. Silva, S. Capdevila, M. García-Vigueras, and J. R. Mosig, "Dual-band circularly polarized transmitarray antenna for satellite communications at (20, 30) GHz," *IEEE Trans. Antennas Propag.*, vol. 67, no. 8, pp. 5325–5333, Aug. 2019, doi: 10.1109/TAP.2019.2912495.

[21] F. F. Manzillo, A. Clemente, and J. L. González-Jiménez, "High-Gain D-band transmitarrays in standard PCB technology for beyond-5G communications," *IEEE Trans. Antennas Propag.*, vol. 68, no. 1, pp. 587–592, Jan. 2020, doi: 10.1109/TAP.2019.2938630.

[22] C. Xue, Q. Lou, and Z. N. Chen, "Broadband double-layered Huygens' metasurface lens antenna for 5G millimeter-wave systems," *IEEE Trans. Antennas Propag.*, vol. 68, no. 3, pp. 1468–1476, Mar. 2020, doi: 10.1109/TAP.2019.2943440.

[23] S. Li, Z. N. Chen, T. Li, F. H. Lin, and X. Yin, "Characterization of metasurface lens antenna for sub-6 GHz dual-polarization full-dimension massive MIMO and multibeam systems," *IEEE Trans. Antennas Propag.*, vol. 68, no. 3, pp. 1366–1377, Mar. 2020, doi: 10.1109/TAP.2020.2968849.

[24] L. Di Palma, A. Clemente, L. Dussopt, R. Sauleau, P. Potier, and P. Pouliguen, "Radiation pattern synthesis for monopulse radar applications with a reconfigurable transmitarray antenna," *IEEE Trans. Antennas Propag.*, vol. 64, no. 9, pp. 4148–4154, Sep. 2016, doi: 10.1109/TAP.2016.2586491.

[25] A. H. Abdelrahman, F. Yang, A. Z. Elsherbeni, and P. Nayeri, "Analysis and design of transmitarray antennas," *Synth. Lect. Antennas*, vol. 6, no. 1, pp. 1–175, Jan. 2017, doi: 10.2200/S00749ED1V01Y201612ANT012.

[26] A. H. Abdelrahman, A. Z. Elsherbeni, and F. Yang, "Transmission phase limit of multilayer frequency-selective surfaces for transmitarray designs," *IEEE Trans. Antennas Propag.*, vol. 62, no. 2, pp. 690–697, Feb. 2014, doi: 10.1109/TAP.2013.2289313.

[27] S. B. Glybovski, S. A. Tretyakov, P. A. Belov, Y. S. Kivshar, and C. R. Simovski, "Metasurfaces: From microwaves to visible," *Phys. Rep.*, vol. 634, pp. 1–72, May 2016, doi: 10.1016/j.physrep.2016.04.004.

[28] F. A. Dicandia and S. Genovesi, "Linear-to-circular polarization transmission converter exploiting meandered metallic slots," *IEEE Antennas Wireless Propag. Lett.*, vol. 21, no. 11, pp. 2191–2195, Nov. 2022, doi: 10.1109/LAWP.2022.3188063.

[29] X. Dai, G.-B. Wu, and K.-M. Luk, "A wideband circularly polarized transmitarray antenna for millimeter-wave applications," *IEEE Trans. Antennas Propag.*, vol. 71, no. 2, pp. 1889–1894, Feb. 2023, doi: 10.1109/TAP.2022.3215252.

[30] F. Zhang, G.-M. Yang, and Y.-Q. Jin, "Low-profile circularly polarized transmitarray for wide-angle beam control with a third-order meta-FSS," *IEEE Trans. Antennas Propag.*, vol. 68, no. 5, pp. 3586–3597, May 2020, doi: 10.1109/TAP.2020.2964957.

[31] Z. H. Jiang, F. Wu, T. Yue, and W. Hong, "Wideband and low-profile integrated dual-circularly-polarized transmit-arrays enabled by antenna-filter-antenna phase shifting cells," *IEEE Trans. Antennas Propag.*, vol. 69, no. 11, pp. 7462–7475, Nov. 2021, doi: 10.1109/TAP.2021.3076586.

[32] Z. H. Jiang, L. Kang, T. Yue, W. Hong, and D. H. Werner, "Wideband transmit arrays based on anisotropic impedance surfaces for circularly polarized single-feed multibeam generation in the Q-band," *IEEE Trans. Antennas Propag.*, vol. 68, no. 1, pp. 217–229, Jan. 2020, doi: 10.1109/TAP.2019.2943343.

[33] X. Zhang, F. Yang, S. Xu, A. Aziz, and M. Li, "Dual-layer transmitarray antenna with high transmission efficiency," *IEEE Trans. Antennas Propag.*, vol. 68, no. 8, pp. 6003–6012, Aug. 2020, doi: 10.1109/TAP.2020.2989555.

[34] P. K. T. Rajanna, K. Rudramuni, and K. Kandasamy, "A high-gain circularly polarized antenna using zero-index metamaterial," *IEEE Antennas Wireless Propag. Lett.*, vol. 18, no. 6, pp. 1129–1133, Jun. 2019, doi: 10.1109/LAWP.2019.2910805.

[35] K. Liu, G. Wang, T. Cai, W. Guo, Y. Zhuang, and G. Liu, "Ultra-thin circularly polarized lens antenna based on single-layered transparent metasurface," *Chin. Phys. B*, vol. 27, no. 8, Aug. 2018, Art. no. 84101, doi: 10.1088/1674-1056/27/8/084101.

[36] B. Xiang, X. Dai, and K.-M. Luk, "A wideband 2-bit transmitarray antenna for millimeter-wave vehicular communication," *IEEE Trans. Veh. Technol.*, vol. 71, no. 9, pp. 9202–9211, Sep. 2022, doi: 10.1109/TVT.2022.3178843.

[37] H. Yu, J. Su, Z. Li, and F. Yang, "A novel wideband and high-efficiency electronically scanning transmitarray using transmission metasurface polarizer," *IEEE Trans. Antennas Propag.*, vol. 70, no. 4, pp. 3088–3093, Apr. 2022, doi: 10.1109/TAP.2021.3137414.

[38] M. M. Honari, K. Mavrakakis, H. Luyen, J. H. Booske, and N. Behdad, "A dual-band transmitarray antenna employing ultra-thin, polarization-rotating spatial phase shifters," *IEEE Trans. Antennas Propag.*, vol. 70, no. 11, pp. 11132–11137, Nov. 2022, doi: 10.1109/TAP.2022.3184504.

[39] F. Wu, J. Wang, R. Lu, X. Xia, W. Hong, and K.-M. Luk, "Wideband and low cross-polarization transmitarray using 1 bit magnetoelectric dipole elements," *IEEE Trans. Antennas Propag.*, vol. 69, no. 5, pp. 2605–2614, May 2021, doi: 10.1109/TAP.2020.3026904.

[40] K. Mavrakakis, H. Luyen, J. H. Booske, and N. Behdad, "Wideband transmitarrays based on polarization- rotating miniaturized-element frequency selective surfaces," *IEEE Trans. Antennas Propag.*, vol. 68, no. 3, pp. 2128–2137, Mar. 2020, doi: 10.1109/TAP.2019.2949694.

[41] L. Di Palma, A. Clemente, L. Dussopt, R. Sauleau, P. Potier, and P. Pouliguen, "1-bit reconfigurable unit cell for ka-band transmitar-rays," *IEEE Antennas Wireless Propag. Lett.*, vol. 15, pp. 560–563, 2016, doi: 10.1109/LAWP.2015.2458179.

[42] B. Zheng, Y. Fan, and Y. J. Cheng, "Wideband high-efficiency circularly polarized transmitarray with linearly polarized feed," *IEEE Antennas Wireless Propag. Lett.*, vol. 22, no. 6, pp. 1451–1455, Jun. 2023, doi: 10.1109/LAWP.2023.3246046.

[43] F. Wu, J. Wang, R. Lu, L. Xiang, W. Hong, and K.-M. Luk, "A wideband subwavelength-thick circularly polarized discrete lens using dielectric-coated polarization-twisting ME-dipole elements," *IEEE Antennas Wireless Propag. Lett.*, vol. 20, no. 9, pp. 1706–1710, Sep. 2021, doi: 10.1109/LAWP.2021.3094535.

[44] F. Diaby, A. Clemente, K. T. Pham, R. Sauleau, and L. Dussopt, "Circularly polarized transmitarray antennas at ka-band," *IEEE Antennas Wireless Propag. Lett.*, vol. 17, no. 7, pp. 1204–1208, Jul. 2018, doi: 10.1109/LAWP.2018.2839021.

[45] K. T. Pham, A. Clemente, D. Blanco, and R. Sauleau, "Dual-circularly polarized high-gain transmitarray antennas at ka-band," *IEEE Trans. Antennas Propag.*, vol. 68, no. 10, pp. 7223–7227, Oct. 2020, doi: 10.1109/TAP.2020.2996680.

[46] L. Di Palma, A. Clemente, L. Dussopt, R. Sauleau, P. Potier, and P. Pouliguen, "Circularly polarized transmitarray with sequential rotation in ka-band," *IEEE Trans. Antennas Propag.*, vol. 63, no. 11, pp. 5118–5124, Nov. 2015, doi: 10.1109/TAP.2015.2474149.

[47] R. Harrington and J. Mautz, "Theory of characteristic modes for conducting bodies," *IEEE Trans. Antennas Propag.*, vol. 19, no. 5, pp. 622–628, Sep. 1971, doi: 10.1109/TAP.1971.1139999.

[48] F. A. Dicandia and S. Genovesi, "Design of a transmission-type polarization-insensitive and angularly stable polarization rotator by using characteristic modes theory," *IEEE Trans. Antennas Propag.*, vol. 71, no. 2, pp. 1602–1612, Feb. 2023, doi: 10.1109/TAP.2022.3227459.

[49] E. Safin and D. Manteuffel, "Reconstruction of the characteristic modes on an antenna based on the radiated far field," *IEEE Trans. Antennas Propag.*, vol. 61, no. 6, pp. 2964–2971, Jun. 2013, doi: 10.1109/TAP.2013.2251312.

[50] F. A. Dicandia, S. Genovesi, and A. Monorchio, "Null-steering antenna design using phase-shifted characteristic modes," *IEEE Trans. Antennas Propag.*, vol. 64, no. 7, pp. 2698–2706, Jul. 2016, doi: 10.1109/TAP.2016.2556700.

[51] F. A. Dicandia and S. Genovesi, "A compact cubesat antenna with beamsteering capability and polarization agility: Characteristic modes theory for breakthrough antenna design," *IEEE Antennas Propag. Mag.*, vol. 62, no. 4, pp. 82–93, Aug. 2020, doi: 10.1109/MAP.2020.2965015.

[52] J. J. Adams, S. Genovesi, B. Yang, and E. Antonino-Daviu, "Antenna element design using characteristic mode analysis: Insights and research directions," *IEEE Antennas Propag. Mag.*, vol. 64, no. 2, pp. 32–40, Apr. 2022, doi: 10.1109/MAP.2022.3145718.

[53] T. Li and Z. N. Chen, "Metasurface-based shared-aperture 5G S-/K-band antenna using characteristic mode analysis," *IEEE Trans. Antennas Propag.*, vol. 66, no. 12, pp. 6742–6750, Dec. 2018, doi: 10.1109/TAP.2018.2869220.

[54] A. Ericsson and D. Sjöberg, "Design and analysis of a multilayer meander line circular polarization selective structure," *IEEE Trans. Antennas Propag.*, vol. 65, no. 8, pp. 4089–4101, Aug. 2017, doi: 10.1109/TAP.2017.2710207.

[55] K. Kumar Kishor and S. V. Hum, "A pattern reconfigurable chassis-mode MIMO antenna," *IEEE Trans. Antennas Propag.*, vol. 62, no. 6, pp. 3290–3298, Jun. 2014, doi: 10.1109/TAP.2014.2313634.

[56] S. M. A. Momeni Hasan Abadi and N. Behdad, "Wideband linear-to-circular polarization converters based on miniaturized-element frequency selective surfaces," *IEEE Trans. Antennas Propagat.*, vol. 64, no. 2, pp. 525–534, Feb. 2016, doi: 10.1109/TAP.2015.2504999.

[57] T. Li et al., "Characteristic mode inspired dual-polarized double-layer metasurface lens," *IEEE Trans. Antennas Propag.*, vol. 69, no. 6, pp. 3144–3154, Jun. 2021, doi: 10.1109/TAP.2020.3046423.

[58] D. Santillán-Haro, E. Antonino-Daviu, D. Sánchez-Escuderos, and M. Ferrando-Bataller, "Analysis and design of a metamaterial lens antenna using the theory of characteristic modes," *Int. J. Antennas Propag.*, vol. 2018, pp. 1–8, Feb. 2018, doi: 10.1155/2018/6329531.

FRANCESCO ALESSIO DICANDIA (Member, IEEE) was born in Carrara, Italy, in 1988. He received the bachelor's and master's degrees in telecommunications engineering and the Ph.D. degree in information engineering from the University of Pisa, Pisa, Italy, in 2012, 2014, and 2018, respectively. From November 2017 to August 2020, he worked with Greenwaves srl, Milan, Italy, as a Microwave/Antenna Engineer within which he was responsible for several industrial antenna development and projects in the field of 5G systems. From September 2020 to October 2022, he worked with IDS Ingegneria dei Sistemi, Pisa, within the Electromagnetic Engineering Division. Since November 2022, he has been a Researcher with the Institute of Electronics, Information Engineering and Telecommunications, National Research Council (CNR), Pisa. His research activity is mainly focused on characteristic modes analysis, phased arrays, reconfigurable antennas, multiple-input-multiple-output antennas, and radio frequency identification systems. He was a recipient of the Three-Years Grant provided by the Consorzio Nazionale Interuniversitario per le Telecomunicazioni, Pisa, in 2014.

SIMONE GENOVESI (Senior Member, IEEE) received the Laurea degree in telecommunication engineering and the Ph.D. degree in information engineering from the University of Pisa, Pisa, Italy, in 2003 and 2007, respectively. Since 2003, he has been collaborating with the Electromagnetic Communication Laboratory, The Pennsylvania State University, University Park, PA, USA. From 2004 to 2006, he was a Research Associate with the ISTI Institute, National Research Council of Italy (CNR), Pisa. From 2015 to 2017, he was several times a short-term Visiting Researcher with the Grenoble Institute of Technology, Valence, France, and Universitat Rovira I Virgili, Tarragona, Spain. He is currently an Associate Professor with the Dipartimento di Ingegneria dell'Informazione, University of Pisa. He is also the Coordinator of the Additive Manufacturing founded in the framework of the Department of Excellence ("Dipartimenti di Eccellenza") funded by the Italian Ministry of Education, University and Research. His current research topics focus on additive manufacturing, sensors, radio frequency identification systems, and reconfigurable antennas. He is also an Associate Editor of the IEEE TRANSACTIONS ON ANTENNAS AND PROPAGATION.